Distribution Agreement

In presenting this thesis as a partial fulfillment of the requirements for an advanced degree from Emory University, I hereby grant to Emory University and its agents the non-exclusive license to archive, make accessible, and display my thesis in whole or in part in all forms of media, now or hereafter known, including display on the World Wide Web. I understand that I may select some access restrictions as part of the online submission of this thesis. I retain all ownership rights to the copyright of the thesis. I also retain the right to use in future works (such as articles or books) all or part of this thesis.

Signature

_____ _____

Nannan Han

Electron Transfer Kinetics in a Triad Photo-anode for Light-driven Water-splitting

By
Nannan Han
Master of Science
Chemistry Department

_____
Tianquan Lian, PhD
Advisor

_____
Craig L. Hill, PhD
Committee Member

_____
Brian Dyer, PhD
Committee Member

Accepted:

_____
Lisa A. Tedesco, Ph.D.
Dean of the James T. Laney School of Graduate Studies

_____
Date

Electron Transfer Kinetics in a Triad Photo-anode for Light-driven Water-splitting

By

Nannan Han
M.S., Xiamen University
China, 2011

Advisor

Tianquan Lian, Ph. D.

An Abstract of
A thesis submitted to the Faculty of the
James T. Laney Graduate School Studies of Emory University
in partial fulfillment of the requirements for the degree of
Master of Science
in Chemistry
2013

Abstract

Electron Transfer Kinetics in a Triad Photo-anode for Light-driven Water-splitting

By Nannan Han

Efficient water oxidation remains a key challenge for the production of fuel from water. In this report, triadic water oxidizing photoanode has been assembled from nanoporous TiO_2, a novel crown-ether derivative sensitizer $[Ru(5\text{-crownphen})_2(dpb)]^{2+}$ (C2P2) and a polyoxometalate water oxidation catalyst $[\{Ru_4O_4(OH)_2(H_2O)_4\}(\gamma\text{-}SiW_{10}O_{36})_2]^{10-}$ (**POM**). Visible and IR transient absorption measurements were used to monitor and compare the population change of C2P2 and electron injection into TiO_2 in different systems of the C2P2 aqueous solution, C2P2/TiO_2 and **POM**/C2P2/TiO_2 respectively. Electron transfers from catalyst POM to sensitizer C2P2 were confirmed indicated the photogenerated oxidized C2P2 could effectively oxidize **POM** to generate the charge separate state (TiO_2^--C2P2-POM^+) – the first of the four catalyst oxidation events needed for water oxidation. More work unraveling the parameters effects of the system such as pH dependence, power dependence, loading dependence etc. were studied.

Electron Transfer Kinetics in a Triad Photo-anode for Light-driven Water-splitting

By

Nannan Han
M.S., Xiamen University
China, 2011

Advisor: Tianquan Lian, Ph. D.

A thesis submitted to the Faculty of the
James T. Laney Graduate School Studies of Emory University
In partial fulfillment of the requirements for the degree of
Master of Science
in Chemistry

2013

Table of Contents

List of Abbreviations

Abs	Absorbance
C2P2	$[Ru(5\text{-crown-phen})_2(dpb)]^{2+}$ (dpb =4,4'-diphosphonic acid 2,2'bipyridine)
DSSC	Dye Sensitized Solar Cell
ET	electron transfer
FTO	Fluorine doped Tin Oxide
MLCT	Metal-to-ligand charge transfer
P2	$Ru(bpy)_2(4,4'\text{-}PO_3H_2bpy)Cl_2$
POM	Polyoxometalate
PV	Photovoltaic
PVC	Photovoltaic Cell
Ru_4POM	$[Ru^{IV}_4O_4(OH)_2(H_2O)_4\}(\gamma\text{-}SiW_{10}O_{36})_2]^{10-}$
THpA	Tetraheptyl ammonium
UV-Vis	Ultraviolet-Visible

List of Figures

List of Schemes and Tables

Chapter 1:
Introduction

1.1 General Introduction

We depend on fossil fuels to run our vehicles, heat and cool our homes, power manufacturing, and provide us with electricity. However, the fossil fuels induced energy shortage and the environmental pollution push the demands of a cleaner, renewable energy sources more and more urgent. In the past decades, the world made great progress in solar to fuel conversion as shown in table 1.1. The first solar module with an efficiency of 6% was accomplished in Bell Labs in1954, while in 2013 the new record of the solar cell has already achieved an efficiency of 44.7% announced by German Fraunhofer Institute for Solar Energy Systems, Soitec, CEA-Leti and the Helmholtz Center Berlin[1]. Since 1970s energy crisis, the worldwide solar cells production has provided a 1000-fold increase in gigawatts per year and almost a 100-fold increase in billions of U.S. dollars per year in sales; the 2000s energy crisis further spur the solar energy innovation and the cost reduction[2]. Worldwide production exceeded 1GW/year in 2002 and rose to over 3.8GW/year by 2006, and worldwide sales increased from 1.5 to 9.7 billion US$ over this same time period[2]. Like many high-technology and electronic products, the cost reduction of solar cells roughly followed a learning curve of dropping about a factor of 2 for every 10-fold increase in cumulative market production[3].

In spite of the fast development in photovoltaic (PV) field, the complicated manufactured crystalline silicon still dominates the market today and the levelised cost of electricity (LCOE) of PV remains high. To further propel the solar energy conversion, different types of PV systems are hotly studied in recent years, such as DSSC, organic PVC, inorganic PVC, PEC and water-splitting cells[4-9]. New materials and methods were continuously invented and reported[5,8] not only to enhance the

efficiency[10] but also to improve the stability and to reduce the production cost[11]. In parallel with the advances in materials synthesis and discovery, considerable efforts have been devoted to better understand the mechanisms underlying the device performance.[12-16] For examples, electronic coupling[17,18], density of states in the semiconductor [19,20], driving force[21-23] and other parameters[24] that control the interfacial electron transfer rate were separately examined[23,25]; operating condition of solar cells, including excitation intensity[26,27], electrolyte composition[28-30], and the externally applied bias[31,32] were studied and optimized.

Table 1.1 Timeline of solar cells[33]

1839	It is observed that the presence of sunlight is capable of generating usable electrical energy in the 19th century
1905	Albert Einstein publishes a paper explaining the photoelectric effect on a quantum basis.
1920	Solar water-heating systems, utilizing "flat collectors" (or "flat-plate collectors"), relied upon in homes and apartment buildings in Florida and southern California.
1954	First solar modual with efficiency of 6% was accomplished in Bell Labs.
1955	Western Electric licences commercial solar cell technologies. Hoffman Electronics-Semiconductor Division creates a 2% efficient commercial solar cell for $25/cell or $1,785/Watt.
1958	T. Mandelkorn, U.S. Signal Corps Laboratories, creates n-on-p silicon solar cells, which are more resistant to radiation damage and are better suited for space. Hoffman Electronics creates 9% efficient solar cells. Vanguard I, the first solar powered satellite, was launched with a 0.1W, 100 cm² solar panel.
1967	Akira Fujishima discovers the Honda-Fujishima effect which is used for hydrolysis in the photoelectrochemical cell[34].
1976	David Carlson and Christopher Wronski of RCA Laboratories create first amorphous silicon PV cells, which have an efficiency of 1.1%.
1978	First solar-powered calculators.[33]
1980	The Institute of Energy Conversion at University of Delaware develops the first thin film solar cell exceeding 10% efficiency using Cu_2S/CdS technology.
1989	Reflective solar concentrators are first used with solar cells.
1991	Efficient Dye-sensitized solar cell is invented by M. Grätzel etc[35].
1996	The National Center for Photovoltaics is established. Graetzel, École Polytechnique Fédérale de Lausanne, Lausanne, Switzerland achieves 11% efficient energy conversion with dye-sensitized cells that use a photoelectrochemical effect.
2006	For the first time, over half of the world's supply of polysilicon was being used for production of renewable electricity solar power panels.
2007	Google solar panel project begins operation.

2010	BP announces the closing of their photovoltaic plant in Maryland, moving all of their manufacturing work to China.
2011	Fast-growing factories in China push manufacturing costs down to about $1.25 per watt for silicon photovoltaic modules. Installations double worldwide.
2012	3D PV-cel with 30% more energy efficiency
2013	The new record of the solar cell has achieved an efficiency of 44.7% announced by German Fraunhofer Institute for Solar Energy Systems, Soitec, CEA-Leti and the Helmholtz Center Berlin[1]

1.2 Solar Energy Conversion Overview

More energy from sunlight strikes earth in 1 hour than all of the energy consumed by humans in an entire year[36]. Traditionally, we used fossil fuel like coal or petroleum which was converted through millions years from plants or animals which lived on sunlight; nowadays solar cells have already achieved to convert the solar energy to electricity in seconds. The state of the art PVCs and their efficiencies are shown in the table 1.2 and the figure 1.1 from the 2013 NREL data of the Best Research-Cell Efficiencies.

Silicon solar cells, Thin film solar cells and Multijuction solar cells

Today, crystalline silicon PVCs are used in the largest quantity of all types of solar cells on the market. The highest efficiency of this type of PVCs is 25%, while the standard industry cells remain limited to 15-18%[37]. Despite the high efficiency, the crystalline silicon PVCs are expensive due to their complex structures and the lengthy manufacturing processes required for fabrication. For crystalline silicon PVCs a typical optimized thickness are around 200um, while the thin film PVCs is just a few um. Why the thickness is so important to a solar cell? If the film is too thin, then that region will not absorb sufficient sunlight. If the film is too thick, there is a significant chance that the electron and hole (or exciton) diffusion length will be shorter than the film thickness, and that the charge will therefore not be collected at the p-type and n-type heterojunctions.[8] There are mainly three kind of thin film solar

cells with high efficiency, they are CIGS (CuInGaSe2), CdTe, amorphous Si:H. For the first two thin film PVCs, the problem is the toxic elements and the scarce elements are involved. For the later one the efficiency is low. The thin film PVCs has the potential of achieving module fabrication costs of well below1 € /W_p [38].

The most high efficiency solar cells are the multijunction solar cells with an efficiency of 44.7%[1] . What needs to be done to achieve high efficiencies? Three things need to be done. First, for each photon absorbed, the excited state carrier generated needs to last long enough to be collected at the junction. Second, while the sun's spectrum contains photons of different energies, the energy available in each photon must be used as wisely as possible. And third, the voltage a cell generates should be as close as possible to the bandgap energy[2]. How does a multijuction solar cell work? In a two junction solar cell, the high-energy photons was first absorbed in the top material generating a high voltage, while the low-energy photons pass through the top cell to be converted in the bottom cell[2].

Dye sensitized solar cells and organic solar cells

The dye sensitized solar cells (DSSCs) is important PVCs. The major advantage of the concept of dye sensitization is the fact that the conduction mechanism is based on a majority carrier transport as opposed to the minority carrier transport of conventional inorganic cells. This means that bulk or surface recombination of the charge carriers in the TiO2 semiconductor cannot happen. Thus, impure starting materials and a simple cell processing without any clean room steps are permitted, yet resulting in promising conversion efficiencies of 7–11% and the hope of a low-cost device for photoelectrochemical solar energy conversion. On the other hand impure materials can result in a strongly reduced lifetime of the cells. The most important issue of the dye-sensitized cells is the stability over the time and the temperature

range which occurs under outdoor conditions.[39] And Researchers have applied atomic layer deposition (ALD) on DSSC to improve the stability[40]. Beside DSSCs, which may be considered as organic/inorganic hybrid cells, other types of organic solar cells currently become of broader interest. These cells can be divided roughly into molecular and polymer organic solar cells.[41] Before these cells become practical, the efficiency will have to be increased further. Also, long-term stability and protection against environmental influences are significant challenges.[39]

Table 1.2 Highest Efficiency of the typical Solar Cells[42]

typical PVCs	Efficiency	Challenges
single crystal silicon	25.0%	Expensive
Multicrystal silicon	20.4%	Good
InGaP/GaAs/InGaAs multijunction	43.5%	Expensive toxic
GaAs thin film	28.8%	toxic
Cu(In,Ga)Se2 or CIGS	20.3%	toxic
CdTe	18.3%	toxic
amorphous Si:H	12.5%	Low efficiency
DSSC	12.0%	Low efficiency
inorganic cells	11.1%	Low efficiency
organic c	10.6%	Low efficiency
quantum dot cell	7.0%[43]	Low efficiency
perovskite solar cell	15%[5,44]	Promising

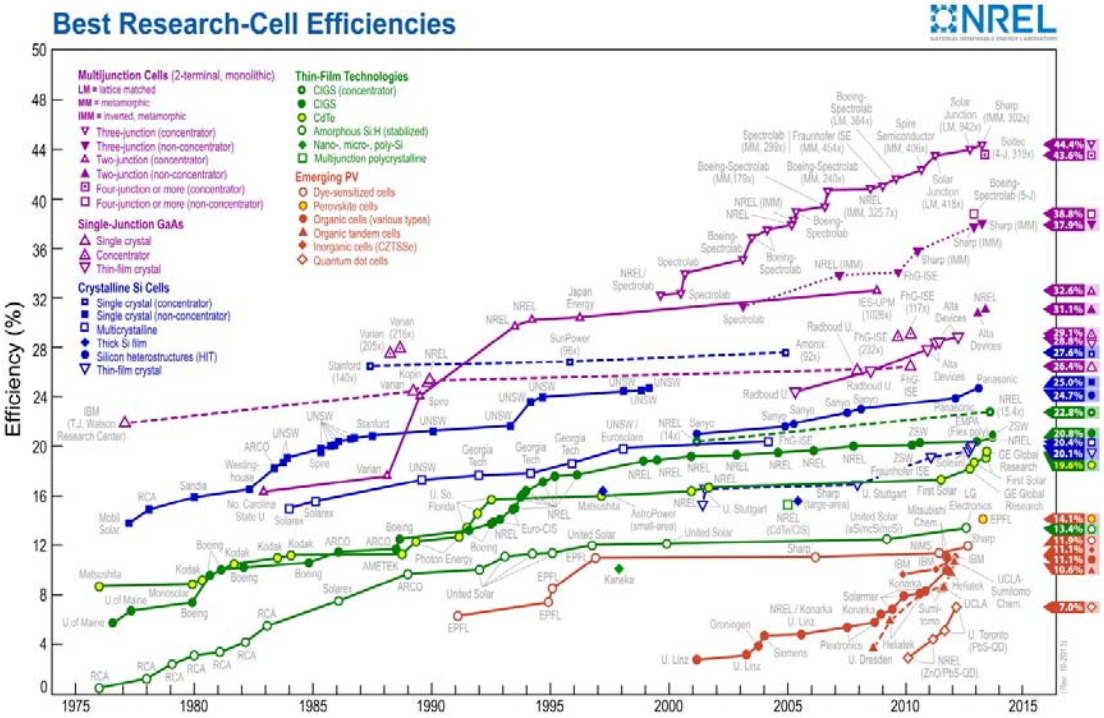

Figure 1.1 Best Research-Cell Efficiencies [45]

Perovskite Materials in solar cells

Currently, perovskite structures (ABX_3) materials ($CH_3NH_3PbI_xCl_{3-x}$, $CH_3NH_3PbI_3$, $CsSnI_{2.95}F_{0.5}$) used in solar cells achieved a great success. In 2012, researcher in Northwestern University published $CsSnI_{2.95}F_{0.5}$ doping material used as p-type layers for hole conduction in lieu of the liquid electrolytes in DSSCs[8] achieved a high efficiency of 10.2%. In 2013, perovskite chromophore $CH_3NH_3PbI_xCl_{3-x}$, $CH_3NH_3PbI_3$ fabricated heterojunction solar cells achieved solar to electrical power conversion efficiencies of over 15%.[46,47] Perovskite materials like $BaSnO_3$ are also used to replace TiO_2 working as photoanode material.[48] $CH_3NH_3PbI_3$ perovskite quantum dot sensitized solar cells also achieved a high efficiency of 6.5%[49]. Researchers in UK, Italy and Singapore using transient absorption and photoluminescence-quenching measurements show that the charge carriers diffusion

lengths are extraordinarily long in the heterojuction perovskite solar cells[50,51].

1.3 Sunlight-Drive Water Splitting

To provide a truly widespread primary energy source, not only solar energy was captured and converted, but also be stored in a cost-effective fashion. One of the possible storage methods is chemical bonds[52]. This leads to the concept of "solar fuels" with targets including water splitting into hydrogen and oxygen and water reduction of CO_2 into almost any form of reduced carbon—CO, formaldehyde, methanol, other oxygenates, methane. Researchers predicted the first solar fuel available in a large amount will be hydrogen because routes to water splitting are more straightforward than reduction of CO_2[53]. The promise of hydrogen as a transportation fuel may be limited because of limitations in on-board hydrogen storage, but hydrogen could be used on site in large-scale power generation. Also, when reacted with CO_2, it is potentially a valuable feed stock for liquid fuels utilizing known technologies[53].

The splitting of H_2O consists of two half reactions: water oxidation to form O_2 and water reduction to form H_2 as shown below:

$$2H_2O \rightarrow O_2 + 4H^+ + 4e^- \quad E = 0.82V, \text{ at pH } 7$$

$$2H^+ + 2e^- \rightarrow H_2 \quad E = 0.41V, \text{ at pH } 7$$

Here E is the reduction potential. Both reactions proceed through multiple proton-coupled electron transfer steps. O_2 formation is a four-electron oxidation process with a high redox potential of 0.82 V vs NHE at pH 7, which makes water oxidation significantly more difficult than water reduction, which requires only 0.41 V vs NHE at pH 7.[54-56] Recent years, a series of carbon-free, all inorganic water oxidizing polyoxomelates have been reported and they represent a very promising family of catalysts for large-scale water splitting in the future[57-60]. In this thesis, one of my projects focuses on studying the electron transfer (ET) kinetics of the all inorganic

water oxidation catalyst **[{$Ru_4O_4(OH)_2(H_2O)_4Re(\gamma\text{-}SiW_{10}O_{36})_2$]$^{10-}$(POM)** and chromophore fabricated water splitting photoanodes (See Chapter 3).

1.4 Pump-Probe Transient Absorption Measurement

In our study, the pump-probe transient absorption technique is the main measurements used to detect the electron transfer (ET) kinetics. Briefly, pump-probe transient absorption measurement is a short pump pulse excites the sample and triggers the photoinduced events under investigation and the second pulse, a panchromic probe pulse with a certain spectral range, probes the sample after a certain delay time as shown in Scheme 1.1. [61] With broad-band probe pulses, this technique allows for simultaneous spectroscopic identification of multiple species (ground, excited, oxidized, and reduced states) of the electron donor and acceptor present at a given time delay after optical excitation. The measured transient spectra as a function of time enables the direct measurement of charge transfer kinetics.[54,61]

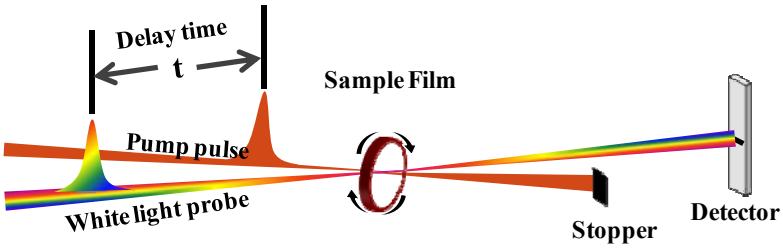

Scheme 1.1 Schematic representation of pump−probe transient absorption measurement.

1.5 Summary of the Projects in the Thesis

In this thesis, I will focus on two parts. The first one is the electron transfer study of the all inorganic water oxidation catalyst **[{$Ru_4O_4(OH)_2(H_2O)_4Re(\gamma\text{-}SiW_{10}O_{36})_2$]$^{10-}$(POM)** and chromophore fabricated water splitting photoanodes. The

other is the study of electron transfer study of the covalent POM–photosensitizer dyads.

In project part I (chapter 3), we have built a triadic photoanode from nanoporous TiO_2, a novel crown-ether derivative sensitizer $[Ru(5\text{-crownphen})_2(dpb)]^{2+}$ (C2P2) which can anchor to TiO_2 surfaces by phosphate groups, and the **first-reported polyoxometalate water oxidation catalyst $[\{Ru_4O_4(OH)_2(H_2O)_4Re(\gamma\text{-}SiW_{10}O_{36})_2]^{10-}$(POM)** which can attach to the C2P2 sensitizer presumably via electrostatic interaction. Visible transient absorption spectroscopy was used to monitor the population of C2P2 sensitizer, while mid IR transient absorption spectroscopy was used to monitor the electrons injected into TiO_2.Combining these two techniques, all the charge-transfer processes in the triad can be investigated. Electron transfer from C2P2 to TiO_2 was confirmed by comparing with control samples of C2P2/ZrO_2 and N3/TiO_2. **POM** oxidation by oxidized state of C2P2 was studied by comparing with C2P2/TiO_2 and control sample $SiW_{12}O_{40}$ (**SiW12**)/C2P2/TiO_2. Therefore, we have observed the desirable triadic charge separated states (TiO_2^--C2P2-**POM**$^+$), which is critical for heterogeneous water oxidation by the TiO_2-C2P2-**POM** photoanode. In the project part II (chapter 4), we have studied the internal electron transfer of the four covalent POM–photosensitizer dyads.

Reference

1 Bett, A. W. *et al.* OVERVIEW ABOUT TECHNOLOGY PERSPECTIVES FOR HIGH EFFICIENCY SOLAR CELLS FOR SPACE AND TERRESTRIAL APPLICATIONS. (2013).

2 Fraas, L. M. & Partain, L. D. *Solar cells and their applications*. Vol. 236 (Wiley. com, 2010).

3 Wallace, W. Government terrestrial acceleration programs. *Solar Cells and Their Applications, Ed. Larry D. Partain, John Wiley & Sons, Inc., New York* (1995).

4 Bakulin, A. A. *et al.* The role of driving energy and delocalized states for charge separation in organic semiconductors. *Science* **335**, 1340-1344 (2012).

5 Burschka, J. *et al.* Sequential deposition as a route to high-performance perovskite-sensitized solar cells. *Nature* **499**, 316-319 (2013).

6 Chen, Z. F. & Meyer, T. J. Copper(II) Catalysis of Water Oxidation. *Angew. Chem.-Int. Edit.* **52**, 700-703, doi:10.1002/anie.201207215 (2013).

7 Chiba, Y. *et al.* Dye-sensitized solar cells with conversion efficiency of 11.1%. *Japanese Journal of Applied Physics Part 2 Letters* **45**, L638 (2006).

8 Chung, I., Lee, B., He, J., Chang, R. P. & Kanatzidis, M. G. All-solid-state dye-sensitized solar cells with high efficiency. *Nature* **485**, 486-489 (2012).

9 Yella, A. *et al.* Porphyrin-Sensitized Solar Cells with Cobalt (II/III)–Based Redox Electrolyte Exceed 12 Percent Efficiency. *Science* **334**, 629-634, doi:10.1126/science.1209688 (2011).

10 Duan, L. L. *et al.* A molecular ruthenium catalyst with water-oxidation activity comparable to that of photosystem II. *Nat. Chem.* **4**, 418-423, doi:10.1038/nchem.1301 (2012).

11 Yin, Q. S. *et al.* A Fast Soluble Carbon-Free Molecular Water Oxidation Catalyst Based on Abundant Metals. *Science* **328**, 342-345, doi:10.1126/science.1185372 (2010).

12 Listorti, A., O'Regan, B. & Durrant, J. R. Electron Transfer Dynamics in Dye-Sensitized Solar Cells. *Chem. Mat.* **23**, 3381-3399, doi:10.1021/cm200651e (2011).

13 Grätzel, M. Recent Advances in Sensitized Mesoscopic Solar Cells. *Accounts of Chemical Research* **42**, 1788-1798, doi:10.1021/ar900141y (2009).

14 O'Regan, B. C. & Durrant, J. R. Kinetic and Energetic Paradigms for Dye-Sensitized Solar Cells: Moving from the Ideal to the Real. *Accounts of Chemical Research* **42**, 1799-1808, doi:10.1021/ar900145z (2009).

15 Ardo, S. & Meyer, G. J. Photodriven heterogeneous charge transfer with transition-metal compounds anchored to TiO(2) semiconductor surfaces. *Chem. Soc. Rev.* **38**, 115-164, doi:10.1039/b804321n (2009).

16 Clifford, J. N., Martinez-Ferrero, E., Viterisi, A. & Palomares, E. Sensitizer molecular structure-device efficiency relationship in dye sensitized solar cells. *Chem. Soc. Rev.* **40**, 1635-1646 (2011).

17 Asbury, J. B., Hao, E., Wang, Y. Q., Ghosh, H. N. & Lian, T. Q. Ultrafast electron transfer dynamics from molecular adsorbates to semiconductor nanocrystalline thin films. *J. Phys. Chem. B* **105**, 4545-4557, doi:10.1021/jp003485m (2001).

18 Asbury, J. B., Hao, E. C., Wang, Y. Q. & Lian, T. Q. Bridge length-dependent ultrafast electron transfer from Re polypyridyl complexes to nanocrystalline TiO2 thin films studied by femtosecond infrared spectroscopy. *J. Phys. Chem. B* **104**, 11957-11964, doi:10.1021/jp002541g (2000).

19 She, C. X. *et al.* pH-dependent electron transfer from re-bipyridyl complexes to metal oxide nanocrystalline thin films. *J. Phys. Chem. B* **109**, 19345-19355, doi:10.1021/jp053948u (2005).

20 Hao, E. C., Anderson, N. A., Asbury, J. B. & Lian, T. Q. Effect of trap states on interfacial electron transfer between molecular absorbates and semiconductor nanoparticles. *J. Phys. Chem. B* **106**, 10191-10198, doi:10.1021/jp021226m (2002).

21 Huang, J., Stockwell, D., Boulesbaa, A., Guo, J. C. & Lian, T. Q. Comparison of electron injection dynamics from rhodamine B to In2O3, SnO2, and ZnO nanocrystalline thin films. *J. Phys. Chem. C* **112**, 5203-5212, doi:10.1021/jp077492n (2008).

22 Stockwell, D. *et al.* Comparison of Electron-Transfer Dynamics from Coumarin 343 to TiO(2), SnO(2), and ZnO Nanocrystalline Thin Films: Role of Interface-Bound Charge-Separated Pairs. *J. Phys. Chem. C* **114**, 6560-6566, doi:10.1021/jp912133i (2010).

23 Asbury, J. B., Anderson, N. A., Hao, E. C., Ai, X. & Lian, T. Q. Parameters affecting electron injection dynamics from ruthenium dyes to titanium dioxide nanocrystalline thin film. *J. Phys.*

Chem. B **107**, 7376-7386, doi:10.1021/jp034148r (2003).
24 She, C. X., Guo, J. C. & Lian, T. Q. Comparison of electron injection dynamics from re-bipyridyl complexes to TiO2 nanocrystalline thin films in different solvent environments. *J. Phys. Chem. B* **111**, 6903-6912, doi:10.1021/jp070561d (2007).
25 Anderson, N. A. & Lian, T. Ultrafast electron injection from metal polypyridyl complexes to metal-oxide nanocrystalline thin films. *Coordination Chemistry Reviews* **248**, 1231-1246, doi:10.1016/j.ccr.2004.03.029 (2004).
26 Durr, M., Menges, B., Knoll, W., Yasuda, A. & Nelles, G. Direct measurement of increased light intensity in optical waveguides coupled to a surface plasmon spectroscopy setup. *Appl. Phys. Lett.* **91**, doi:021113
10.1063/1.2753757 (2007).
27 Durr, M. *et al.* Low-temperature fabrication of dye-sensitized solar cells by transfer of composite porous layers. *Nat Mater* **4**, 607-611, 2005).
28 Haque, S. A. *et al.* Charge separation versus recombination in dye-sensitized nanocrystalline solar cells: the minimization of kinetic redundancy. *J. Am. Chem. Soc.* **127**, 3456-3462, doi:10.1021/ja0460357 (2005).
29 Upadhyaya, H. M., Hirata, N., Haque, S. A., de Paoli, M. A. & Durrant, J. R. Kinetic competition in flexible dye sensitised solar cells employing a series of polymer electrolytes. *Chem. Commun.*, 877-879, doi:10.1039/b515240b (2006).
30 Kambe, S., Nakade, S., Kitamura, T., Wada, Y. & Yanagida, S. Influence of the electrolytes on electron transport in mesoporous TiO2-electrolyte systems. *J. Phys. Chem. B* **106**, 2967-2972, doi:10.1021/jp013397h (2002).
31 Haque, S. A. *et al.* Parameters influencing charge recombination kinetics in dye-sensitized nanocrystalline titanium dioxide films. *J. Phys. Chem. B* **104**, 538-547, doi:10.1021/jp991085x (2000).
32 Tachibana, Y. *et al.* Modulation of the rate of electron injection in dye-sensitized nanocrystalline TiO2 films by externally applied bias. *J. Phys. Chem. B* **105**, 7424-7431, doi:10.1021/jp010173q (2001).
34 Fujishima, A. Electrochemical photolysis of water at a semiconductor electrode. *Nature* **238**, 37-38 (1972).
35 Oregan, B. & Gratzel, M. A LOW-COST, HIGH-EFFICIENCY SOLAR-CELL BASED ON DYE-SENSITIZED COLLOIDAL TIO2 FILMS. *Nature* **353**, 737-740, doi:10.1038/353737a0 (1991).
36 Goldemberg, J. & Johansson, T. B. *World energy assessment: overview: 2004 update*. (United Nations Publications, 2004).
37 Saga, T. Advances in crystalline silicon solar cell technology for industrial mass production. *NPG Asia Materials* **2**, 96-102 (2010).
38 Bloss, W., Pfisterer, F., Schubert, M. & Walter, T. Thin‐film solar cells. *Progress in Photovoltaics: Research and Applications* **3**, 3-24 (1995).
39 Goetzberger, A., Hebling, C. & Schock, H.-W. Photovoltaic materials, history, status and outlook. *Materials Science and Engineering: R: Reports* **40**, 1-46 (2003).
40 Son, H. J. *et al.* Dye Stabilization and Enhanced Photoelectrode Wettability in Water-Based Dye-Sensitized Solar Cells through Post-assembly Atomic Layer Deposition of TiO2. *Journal of the American Chemical Society* **135**, 11529-11532, doi:10.1021/ja406538a (2013).
41 D.Meissner. Plastic Solar Cells. *photon internaional* **2**, 34 (1999).
42 Green, M. A., Emery, K., Hishikawa, Y., Warta, W. & Dunlop, E. D. Solar cell efficiency tables (version 41). *Progress in photovoltaics: research and applications* **21**, 1-11 (2013).
43 Kamat, P. V. Quantum Dot Solar Cells. The Next Big Thing in Photovoltaics. *The Journal of Physical Chemistry Letters* **4**, 908-918, doi:10.1021/jz400052e (2013).
44 Liu, M., Johnston, M. B. & Snaith, H. J. Efficient planar heterojunction perovskite solar cells by vapour deposition. *Nature* **501**, 395-398, doi:10.1038/nature12509 (2013).
46 Liu, M. Z., Johnston, M. B. & Snaith, H. J. Efficient planar heterojunction perovskite solar cells by vapour deposition. *Nature* **501**, 395-+, doi:10.1038/nature12509 (2013).
47 Burschka, J. *et al.* Sequential deposition as a route to high-performance perovskite-sensitized solar cells. *Nature* **499**, 316-+, doi:10.1038/nature12340 (2013).
48 Kim, D. W. *et al.* BaSnO3 Perovskite Nanoparticles for High Efficiency Dye-Sensitized Solar Cells. *ChemSusChem* **6**, 449-454, doi:10.1002/cssc.201200769 (2013).

49 Im, J. H., Lee, C. R., Lee, J. W., Park, S. W. & Park, N. G. 6.5% efficient perovskite quantum-dot-sensitized solar cell. *Nanoscale* **3**, 4088-4093, doi:10.1039/c1nr10867k (2011).
50 Stranks, S. D. *et al.* Electron-Hole Diffusion Lengths Exceeding 1 Micrometer in an Organometal Trihalide Perovskite Absorber. *Science* **342**, 341-344, doi:10.1126/science.1243982 (2013).
51 Xing, G. *et al.* Long-Range Balanced Electron- and Hole-Transport Lengths in Organic-Inorganic CH3NH3PbI3. *Science* **342**, 344-347, doi:10.1126/science.1243167 (2013).
52 Lewis, N. S. Toward cost-effective solar energy use. *Science* **315**, 798-801, doi:10.1126/science.1137014 (2007).
53 Song, W. J. *et al.* Making solar fuels by artificial photosynthesis. *Pure Appl. Chem.* **83**, 749-768, doi:10.1351/pac-con-10-11-09 (2011).
54 Huang, Z. Q., Geletii, Y. V., Musaev, D. G., Hill, C. L. & Lian, T. Q. Spectroscopic Studies of Light-driven Water Oxidation Catalyzed by Polyoxometalates. *Ind. Eng. Chem. Res.* **51**, 11850-11859, doi:10.1021/ie202950h (2012).
55 Walter, M. G. *et al.* Solar water splitting cells. *Chemical reviews* **110**, 6446-6473 (2010).
56 Moore, G. F. & Brudvig, G. W. Energy conversion in photosynthesis: a paradigm for solar fuel production. *Annu. Rev. Condens. Matter Phys.* **2**, 303-327 (2011).
57 Geletii, Y. V. *et al.* An all-inorganic, stable, and highly active tetraruthenium homogeneous catalyst for water oxidation. *Angew. Chem.-Int. Edit.* **47**, 3896-3899, doi:10.1002/anie.200705652 (2008).
58 Besson, C. *et al.* Cs(9) (gamma-PW(10)O(36))(2)Ru(4)O(5)(OH)(H(2)O)(4) , a new all-inorganic, soluble catalyst for the efficient visible-light-driven oxidation of water. *Chem. Commun.* **46**, 2784-2786, doi:10.1039/b926064a (2010).
59 Huang, Z. Q. *et al.* Efficient Light-Driven Carbon-Free Cobalt-Based Molecular Catalyst for Water Oxidation. *J. Am. Chem. Soc.* **133**, 2068-2071, doi:10.1021/ja109681d (2011).
60 Geletii, Y. V. *et al.* Structural, Physicochemical, and Reactivity Properties of an All-inorganic, Highly Active Tetraruthenium Homogeneous Catalyst for Water Oxidation. *J. Am. Chem. Soc.* **131**, 17360-17370, doi:10.1021/ja907277b (2009).
61 Demtröder, W. *Laser Spectroscopy: Vol. 2: Experimental Techniques*. (Springer, 2008).

Resouces from Websites

33 <http://en.wikipedia.org/wiki/Timeline_of_solar_cells>
45 NREL. <http://www.nrel.gov/ncpv/> (2013).

Chapter 2:
Experimental Methods and Preparation of Samples

2.1. Preparation of the Water-Splitting Photoanodes:

Preparation of TiO2 film: TiO2 colloidal nanoparticle films were prepared following Arie Zaban's methods[1]. Briefly, 250 mL of water and 80 mL of acetic acid were added to a 1000 mL round bottom flask and cooled to 0°C. A mixture of 10 mL of 2-propanol and 37 mL of Ti(IV) isopropoxide (Aldrich, 97%) was dropped slowly to the water acetic acid bulk solution over a 30-40 min period under vigorous stirring and dry N_2 purge. After stirring overnight, the transparent colloid was poured into a 1000 ml beaker and heated in 80°C hot water bath for 3-4 h under vigorous stirring. The colloid was autoclaved at 230 °C for 12 h and cooled down to room temperature slowly. After the autoclaving, the gel was separated into liquid and solid phase. About 10ml solid phase was then stirred with 20 drops of TritonX-100(toxic) and then stirred for several days. To make films, clean sapphire windows or FTOs are anchored to the desk by Scotch tape. Several drops of TiO2 colloid was dispersed on the windows and spread by a polished glass rod and then dried in air. The films were baked at 400°C in oven for 3 h.

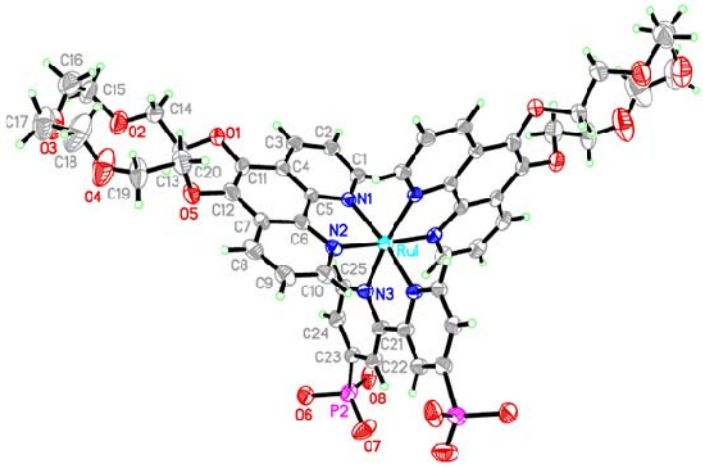

Figure 2.1 The structure of $[Ru(5\text{-crownphen})_2(dpb)]^{2+}$ (C2P2)

Preparation of Dyad (TiO2/C2P2): The photosensitizer $[Ru(5\text{-crownphen})_2(dpb)]^{2+}$ (C2P2) shown in figure 2.1 were synthesized for the first time

by John Fielden. With two phosphate group, the dye can be attached on the TiO2 by electronic attraction. The two crowns are designed to bind cations like sodium ions, and with binding positive ions it may attract more negative charged **POM** into the heterogeneous system. The C2P2 dyad films were made by soaking the TiO2 films in the 10^{-4} M C2P2 (F_w = 1390.19) in 0.1 M $HClO_4$ acetonitrile solution overnight, rinsing with ethanol and drying in air.

*Preparation of **POM**/C2P2/TiO_2 (Triad) and **SiW12**/C2P2/TiO_2:* The polyoxometalate water-oxidation catalyst **$Rb_8K_2[\{Ru_4O_4(OH)_2(H_2O)_4\}\gamma$-$(SiW_{10}O_{36})_2]$(POM)** was synthesized according to the published method[2]. The C2P2 triad films were made by soaking the Dyad films in the **POM** (ca. 2mM) for 30min, rinsing with ethanol and drying in air. The structure scheme is shown in figure 2.2. The control sample was made by the same procedure but replace **POM** by the $SiW_{12}O_{40}$ tetrabutylammonium (TBA) salt (**SiW12**).

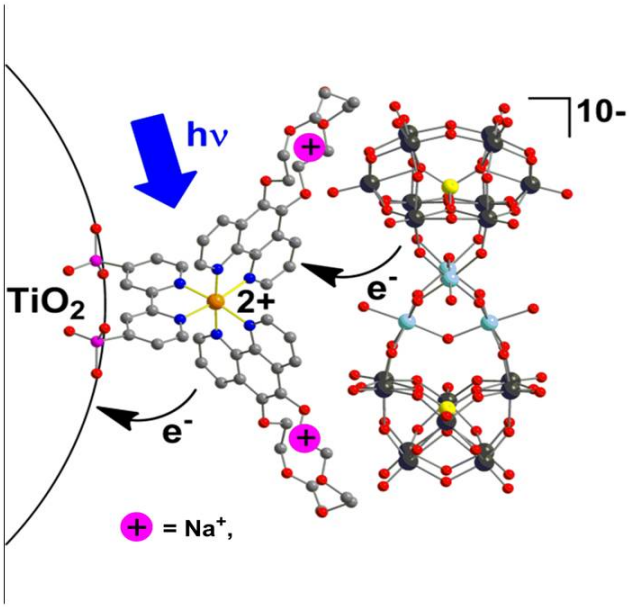

Figure 2.2 the scheme of the **POM**/C2P2/TiO2 heterogeneous system

Soak Dyad films in desired ions: Dyad films were soaking in 0.2 M acetonitrile solutions of $NaClO_4$ or $Mg(ClO_4)_2$ around 30 min.

2.2. The Covalent POM–Photosensitizer Dyads Samples

Four samples of the covalent POM–photosensitizer dyads are used in the transient absorption measurement as shown in figure 2.3. These covalent POM–photosensitizer dyads were synthesized for the first time by Anna Proust Group[3]. In the following text, we use the labeling K and D to refer to the Keggin and Dawson type anions, and Si and Sn to indicate the primary functionalization by sily-aryl or tin-aryl. The structure and the abbreviations of the four covalent POM–photosensitizer dyads and the Ir-photosensitizer are shown in figure 4. K-Si, K-Sn, D-Si, D-Sn refer to the dyads of 3TBA • $[PW_{11}O_{40}\{Si(Aryl)\}_2]^{3-}$_cyclometalated iridium, and 4TBA • $[PW_{11}O_{39}\{Sn(Aryl)\}]^{4-}$_cyclometalated iridium unit, 6TBA • $[P_2W_{17}O_{61}\{Si(Aryl)\}_2]^{6-}$_cyclometalated iridium unit, 7TBA • $[P_2W_{17}O_{61}\{Sn(Aryl)\}]^{7-}$ _cyclometalated iridium unit. The Ir-photosensitizer and the four covalent POM–photosensitizer dyads used to measure the electron transfer kinetics were solved in deoxygenated dimethylformamide (DMF) by argon.

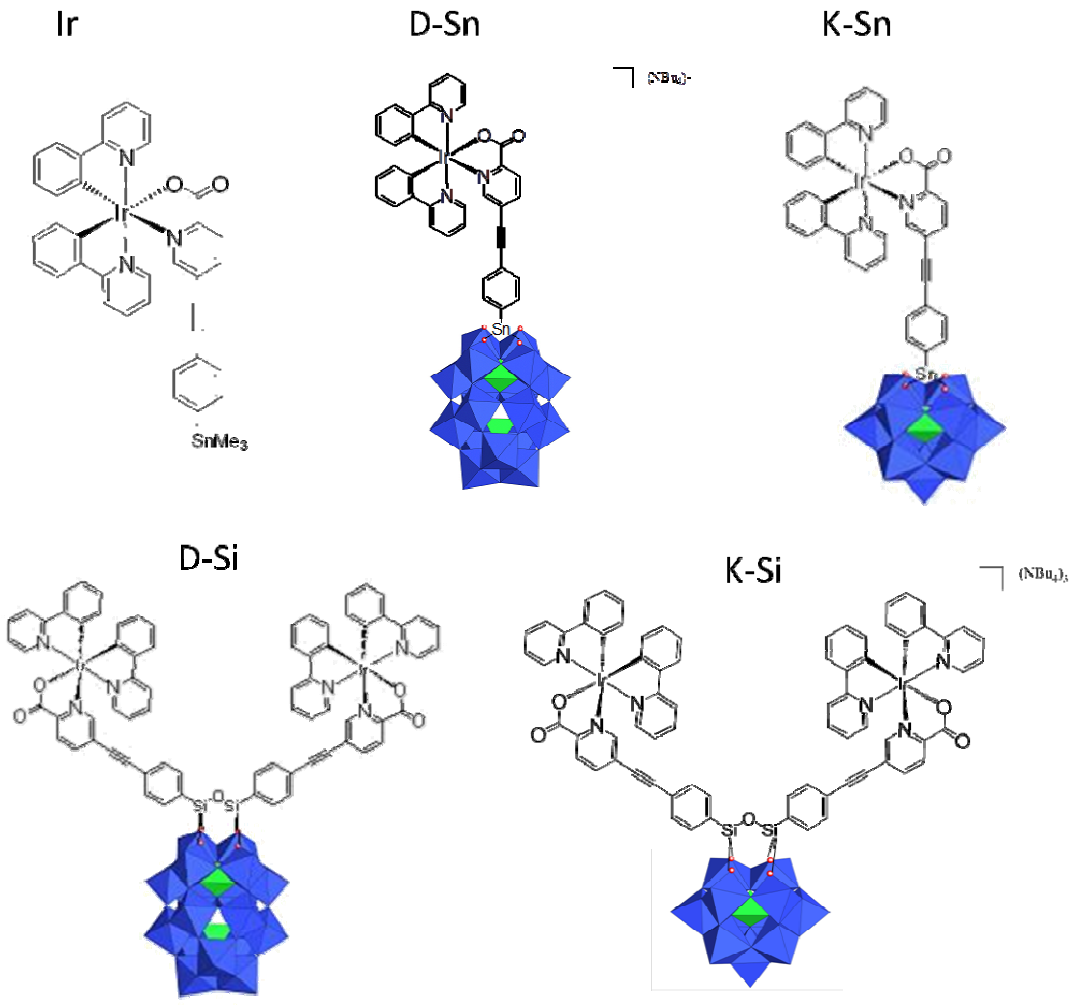

Fig.2.3 The scheme of the structure of the Ir-photosensitizer and the four covalent POM-photosensitizer compounds.

2.3. Pump-probe Transient Absorption Spectroscopy

Femtosecond Transient Absorption (TA) The laser source used in femtosecond transient absorption (TA) is a regeneratively-amplified Ti:sapphire laser system (Coherent Legend, 800 nm, 150 fs, 3 mJ/pulse, and 1 kHz repetition rate) and the spectrometer is Helios (Ultrafast Systems LLC). The pump beam (400 nm) is generated by frequency doubling of the 800 nm pulse from the amplifier in a BBO crystal. A series of neutral-density filter wheels are used to adjust the power of the 400 nm pump beam. The pump beam is focused at the sample with a beam waist of about

300 μm. A white light continuum (WLC) from 420 to 800 nm is generated by attenuating and focusing ~10 μJ of the 800 nm pulse into a sapphire window. The WLC is splitted into a probe and reference beam. The probe beam was focused with an Aluminum parabolic reflector onto the sample (with a beam waist of 150 μm at the sample). The reference and probe beams are focused into a fiber optics-coupled multichannel spectrometer with complementary metal-oxide-semiconductor (CMOS) sensors and detected at a frequency of 1 kHz. The intensities of the pump and probe beams are ratioed to correct for pulse-to-pulse fluctuation of the white-light continuum. The delay between the pump and probe pulses is controlled by a motorized delay stage. The pump beam is chopped by a synchronized chopper to 500 Hz. The change in absorptions for the pumped and unpumped sample is calculated. During the data collection, samples were constantly translated to avoid photodegredation.

Nanosecond Transient Absorption (TA) Nanosecond TA is performed with the EOS spectrometer (Ultrafast Systems LLC). The pump beam at 400 nm is generated in the same way as femtosecond TA experiments. The white light continuum (WLC) from 380 nm to 1700 nm (0.5 ns pulse width, 20 kHz repetition rate) used here is generated by focusing a Nd:YAG laser into a photonic crystal fiber. The delay time between the pump and probe beam is controlled by a digital delay generator (CNT-90, Pendulum Instruments). The probe and reference beams are detected with the same multichannel spectrometers used in femtosecond TA experiments. During the data collection, samples were constantly translated to avoid photodegredation.

Mid IR Transient Absorption Ultrafast absorption experiments were conducted by using pump-probe transient absorption. The tunable infrared spectrometer used a regeneratively amplified Ti:Sapphire laser system (Coherent

Legend, 800 nm, 150 fs, 2.5 mJ/pulse, 1 KHz repetition rate) and two optical parametric amplifiers (OPAs). The 800 nm pump (1 mJ/pulse) was used to pump an IR-OPA (Coherent OPerA) to produce signal and idler outputs at 1380 nm and 1903 nm, respectively. Tunable mid-IR probe pulses were produced by difference-frequency generation of the signal and idler which were collinearly mixed in an AgGaS2 crystal. The probe pulses have a full width at half maximum (FWHM) of ~ 120 cm^{-1} and ~5 μJ energy at 5000 nm. The IR probe pulses were attenuated with a beam splitter and ND filters (to ~10 nJ) and chirp-corrected with Ge windows before the sample. Pump pulses were generated by a home-built sum frequency setup, in which either the signal or idler outputs (80 and 40 μJ, respectively) of an IR-OPA (Clark-MXR, pumped with 1 mJ of 800nm pulse) were collinearly mixed with the 800 nm beam (~100 μJ) in a BBO crystal to produce tunable pump pulses from 460 nm to 650 nm. The energy of the 515 nm pulse used for the measurement was controlled by a variable neutral density filter wheel. After the sample, the probe (centered at 2000 cm^{-1}) was dispersed in a spectrometer with resolution of 15 nm (5.4 cm^{-1} at 2000 cm^{-1}) and detected with a 32-element mercury cadmium telluride (MCT) array detector. Every other pump pulse was blocked by a synchronized chopper (New Focus 3500) at 500 Hz, and the absorbance change was calculated from sequential pumped vs. unpumped probe pulses. The instrument response function and zero time delay were determined with a thin Si wafer, which gives an instantaneous mid-IR absorption response after excitation at 515 nm. Typically, the instrument response function was well fit by a Gaussian function with 160 fs FWHM.

Reference

1 Zaban, A., Ferrere, S., Sprague, J. & Gregg, B. A. pH-dependent redox potential induced in a sensitizing dye by adsorption onto TiO2. *The Journal of Physical Chemistry B* **101**, 55-57 (1997).

2 Geletii, Y. V. *et al.* An all-inorganic, stable, and highly active tetraruthenium homogeneous catalyst for water oxidation. *Angew. Chem.-Int. Edit.* **47**, 3896-3899, doi:10.1002/anie.200705652 (2008).

3 Matt, B. *et al.* Long lived charge separation in iridium(iii)-photosensitized polyoxometalates: synthesis, photophysical and computational studies of organometallic-redox tunable oxide assemblies. *Chemical Science* **4**, 1737-1745 (2013).

Chapter 3 Part I:
The Study of Electron Transfer Process in Water-oxidizing POM/C2P2/TiO_2 Triad Photoanodes

Recent years, a series of carbon-free, all inorganic water oxidizing polyoxomelates have been reported and they represent a very promising family of catalysts for large-scale water splitting in the future[1-4]. In previous studies, water oxidation processes were measured in homogeneous photocatalytic systems to evaluate the turn-over capability of these catalysts[1,5]. However, sacrificial electron acceptors (such as $S_2O_8^{2-}$) were used in these systems. To avoid sacrificial electron acceptors, it is necessary to assemble a photocatalytic electrode in which the photo-generated electrons in the sensitizer can be accepted by, for example, nanoporous TiO_2 as the case in DSSCs. In this work, we have built a triadic photoanode from nanoporous TiO_2, a novel crown-ether derivative sensitizer $[Ru(5\text{-crownphen})_2(dpb)]^{2+}$ (C2P2) which can anchor to TiO_2 surfaces by phosphate groups, and the first-reported polyoxometalate water oxidation catalyst $\mathbf{[\{Ru_4O_4(OH)_2(H_2O)_4Re(\gamma\text{-}SiW_{10}O_{36})_2]^{10-}}$(**POM**) which can attach to the C2P2 sensitizer presumably via electrostatic interaction. Visible transient absorption spectroscopy was used to monitor the population of C2P2 sensitizer, while mid IR transient absorption spectroscopy was used to monitor the electrons injected into TiO_2.Combining these two techniques, all the charge-transfer processes in the triad can be investigated. Electron transfer from C2P2 to TiO_2 was confirmed by comparing with control samples of C2P2/ZrO_2 and N3/TiO_2. **POM** oxidation by oxidized state of C2P2 was studied by comparing with C2P2/TiO_2 and control sample $SiW_{12}O_{40}$ (**SiW12**)/C2P2/TiO_2.

3.1 Transient Absorption Spectra of the C2P2/TiO_2 (Dyad)

Electron transfer (ET) process can be measured by monitoring the spectral changes of the C2P2 sensitizer in the visible region and the mid IR absorption of

injected electrons into TiO_2.[6] Before studying the kinetics of dyad samples, the chromophore C2P2 molecules in water are measured by transient absorption technique as shown in figure 3.1. The negative feature at 405-500 nm is the ground state bleach; the positive signal within 500-600 nm is absorption of the exited state of C2P2. The ground state bleach decay signals are agree with the excited state decay kinetics as shown in figure 3.1(right). The lifetime of the excited state of C2P2 was about 685ns as shown in scheme 3.1 analyzed by fitting the kinetics

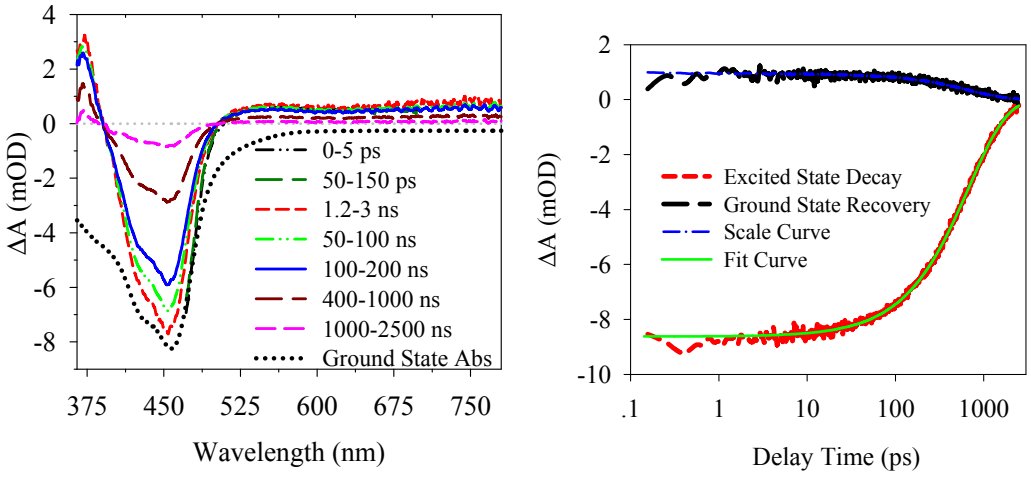

Figure 3.1 (left) Transient Absorption Spectra of C2P2 aqueous solution at indicated delay times after excitation at 400 nm. The dashed line is the ground-state absorption of C2P2 aqueous solution. **(right)** The red line is the ground state bleach of C2P2 in the aqueous solution averaged over 410-480 nm. The black line is the excited state signal of C2P2 averaged over 570-760nm. The blue line is the scaled ground state recovery kinetics, it agrees with excited state decay. The agreement indicates the pure excited state decay process as shown in the following scheme. The green line is fitted with single exponential decay with a lifetime of 685 ns.

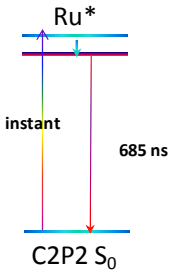

Scheme 3.1 The Schematic electron transfer process of C2P2 in aqueous solution

The statics absorption of the film samples are shown in figure 3.2. Figure 3.3

shows the Transient Absorption Spectrum of C2P2/TiO_2 in the visible region. The dashed line is the scaled static absorption spectrum of C2P2/TiO_2 and the negative feature at 405-500 nm is the ground state bleach; the positive signal within 500-600 nm at earlier time is due to the exited state of C2P2; the broad band from 700 to 900 nm after 1 ns is induced by the C2P2 cation absorption. The kinetics of transient absorption at 534-535 nm (isosbestic point of cation absorption and ground state bleach) and the injected electrons observed in the mid IR are compared as shown in figure 3.4. The agreement of the kinetics of the excited state decay and the electron injection indicates that the decrease of absorption at 500-600 nm at earlier times is caused by the electron injection from excited state of C2P2 to TiO_2 as shown in scheme_1. The injection rate was fitted by two exponential as equation 3.1, where N^- (t) represents the population of injected electrons into TiO_2, N_0 is the population of excited states of C2P2 and the amplitude weighted lifetime is about 95 ps calculated by equation 3.2.

$$N^-(t) = N_0\left[1 - A\times e^{-t/t1} - (1-A)\times e^{-t/t2}\right] \quad \text{----------equation 3.1}$$

$$t = A\times t1 + (1-A)\times t2 \quad \text{----------equation 3.2}$$

A comparison of the ground state bleach decay at 405-500 nm and the C2P2 cation signal decay at 700-900 nm is shown in figure 3.5. It shows that the kinetics of these two processes agrees with each other and they may indicate a charge recombination process as shown in scheme 3.2 (the black arrow) with a half lifetime of the decay is approximately 1.3 us. The injection quantum yield of C2P2 on TiO2 was measure using N3 as reference, as shown in figure 3.6. Figure 3.6 left is the static UV-Vis absorption of the C2P2/TiO2 and the N3/TiO2; comparing the electron injection rates of the two samples, we found that at the eariler time electrons from N3 injected into TiO2 faster than the C2P2, but at the later time the quantum yield of

C2P2 was as much as N3 as shown in figure 3.6 (right).

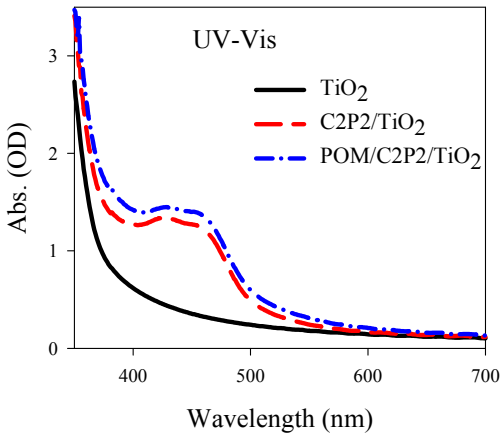

Figure 3.2 UV-vis absorption spectra of TiO_2 (black), TiO_2-C2P2 (red) and TiO_2-C2P2-**POM** (blu

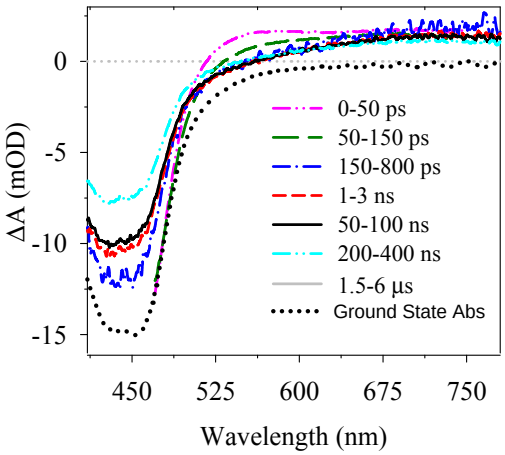

Figure 3.3 Transient Absorption Spectra of C2P2/TiO_2 from 0.15 ps to 6 us. The dashed line is the scaled static absorption of C2P2/TiO_2.

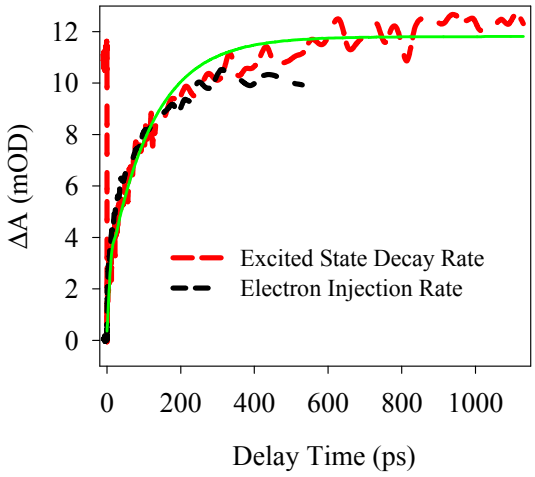

Figure 3.4 Comparison of the scaled kinetics at 534 nm and the electron injection kinetics of mid IR

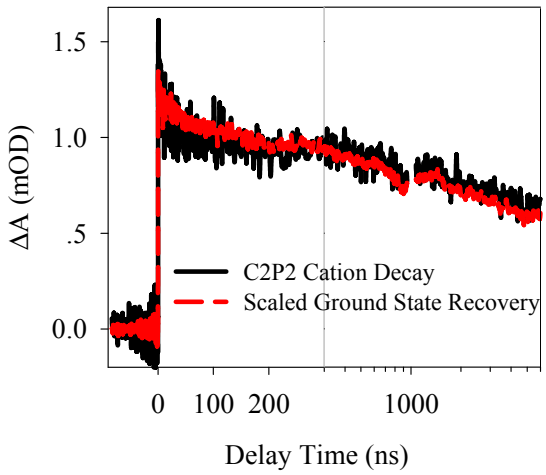

Figure 3.5 The black line is the kinetics of C2P2 cation averaging from 660 nm to760 nm; the red line is the scaled C2P2 ground state kinetics from 470 nm to 475 nm. The agreement of the kinetics indicates the process of the charge recombination and it has a half life time of approximate 1.3 us.

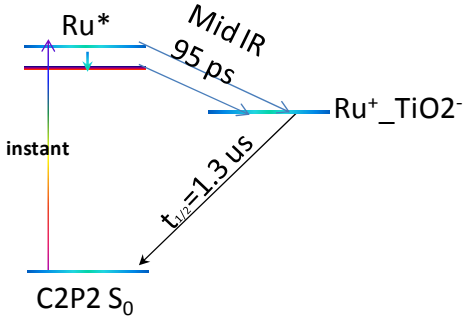

Scheme 3.2. Energy levels and Proposed Electron Transfer process of the C2P2/TiO2

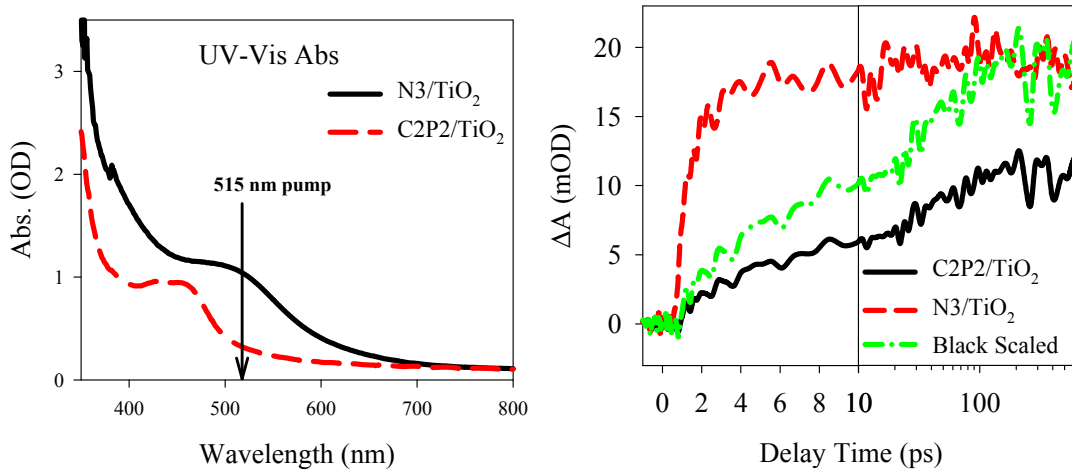

Figure 3.6 (left) The static UV-Vis absorption of $N3/TiO_2$ film and $C2P2/TiO_2$ film. (right) Electron injection kinetics of $N3/TiO_2$ and $C2P2/TiO_2$ films measured by transient Ir absorption (5um) pumped at 515nm. The green line is $C2P2/TiO_2$ kinetics scaled by the number of absorbed photons.

3.2 Transient Absorption Spectra of the POM/C2P2/TiO_2 (Triad)

Transient spectra in the visible region in the presence of **POM** or **SiW12** (the control sample) are shown in figure 3.7. The assignments of the spectra are the same as the C2P2/TiO_2 system because there is no obvious transient absorption signal from the **POM** and **SiW12**. The ground state bleach kinetics of C2P2/TiO_2, **SiW12**/C2P2/TiO_2 and **POM**/C2P2/TiO_2 are shown in figure 3.8. The recovery of the ground state bleach becomes faster in the presence of the **SiW12** than C2P2/TiO_2, as shown in figure 3.8 red line. This is likely due to the electrons of C2P2 excited state transferred to **SiW12** and recovered fast. Figure 3.9 is the comparison of electron injection rates of C2P2/TiO_2, **SiW12**/C2P2/TiO_2 and **POM**/C2P2/TiO_2. In the presence of **SiW12**, 19% of electrons injection population is lost, indicating the electron transfer from C2P2 to **SiW12**; On the other hand the ground state bleaches recovery accelerated and a population of approximately 18% electrons show up (figure 3.8) and this agreement confirmed that the electrons of C2P2 excited state transferred to **SiW12** and recovered fast. The recovery of the ground state bleach becomes much faster in the presence of the **POM**, as shown in figure3.8 (green line). The faster decay of the ground state bleach is mainly caused by electron transfer from the **POM** to the oxidized C2P2. This agrees with the homogeneous system electron transfer process and the transient mid IR data further confirmed this assignment. The transient mid IR kinetics shows that the electron injection into TiO_2 from **POM**/C2P2/TiO_2 is similar as **SiW12**/C2P2/TiO_2. However, the ground state bleach recovery is much faster, and approximately 90% C2P2 recover within 100 ns suggesting that the faster ground state recovery arises from the electron transfer from **POM** to oxidized C2P2.

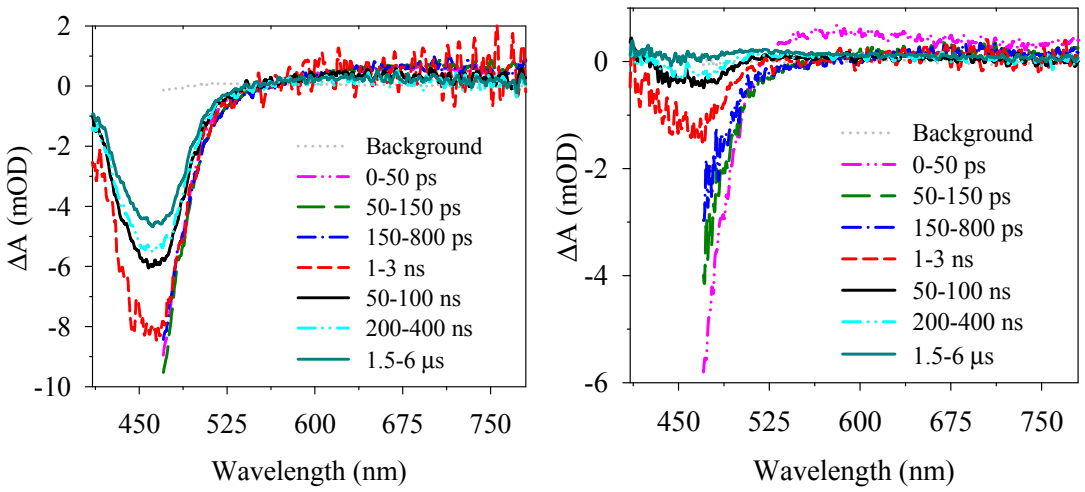

Figure 3.7 Transient absorption spectra of **POM**/C2P2/TiO_2. The dashed line is the scaled static absorption of **POM**/C2P2/TiO_2.

Scheme 3.3 Energy levels and Proposed Electron Transfer process of **POM**/C2P2/TiO2

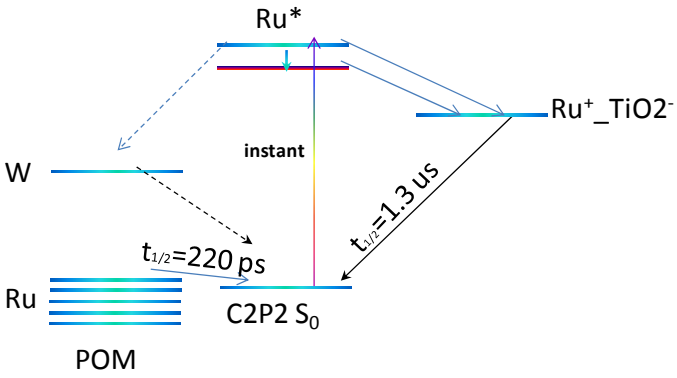

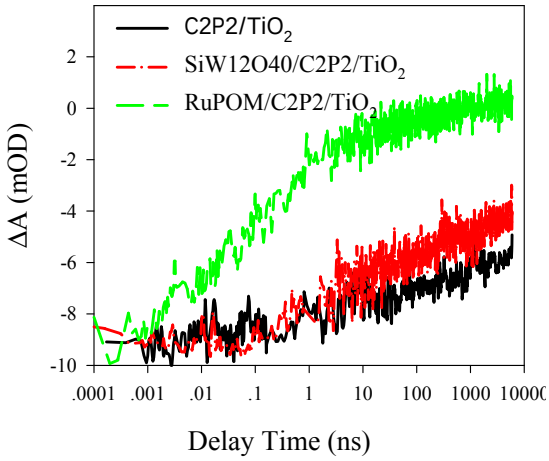

Figure 3.8 The comparison of the ground state bleach kinetics between the C2P2/TiO_2 (the black line), **SiW12**/C2P2/TiO_2 (the red line) and **POM**/C2P2/TiO_2 (the green line) at 470-475 nm

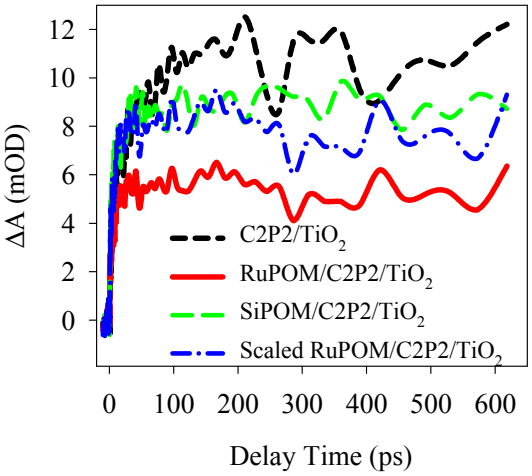

Figure 3.9 The comparison of electron injection rates of C2P2/TiO_2, **SiW12**/C2P2/TiO_2 and **POM**/C2P2/TiO_2 measured by mid-IR transient absorption pumped at 515nm. The blue dash line was scaled by the number of absorbed photons at 515nm. In the presence of **SiW12** or **POM**, about 19% of the population of electrons injection lost, indicating the electron transfer from C2P2 to **SiW12** or **POM.**

3.3 Parameters affecting ET from the catalyst POM to C2P2.

3.3.1 pH dependence

Protonate level of POM would affect the charge transfer processes in the **POM**/C2P2/TiO_2 triad system while with the control sample, C2P2/TiO2 dyad films, there are no obvious difference. The data shows that the sample rinsed by $HClO_4$ solution with different pH have significantly different electron transfer rate from **POM** to C2P2 as shown in the figure 3.10.

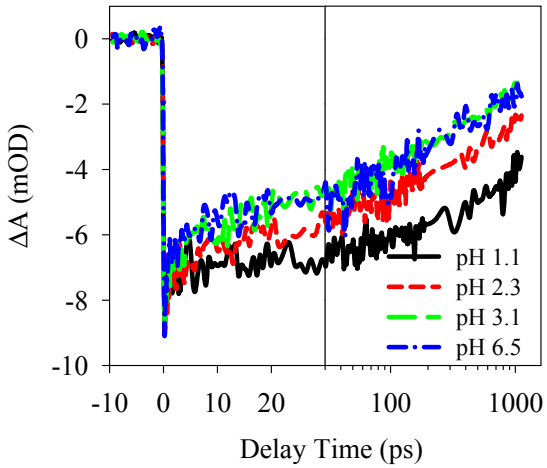

Figure 3.10 The comparison of the ground state recovery kinetics of **POM**/C2P2/TiO_2 after the film is rinsed by the different pH $HClO_4$ solution.

3.3.2 Power dependence of the dyad and the triad

We have performed power dependence experiments on the dyad and the triad samples. The results show that for the triad systems there were no power dependence of the electron transfer from **POM** to oxidized chromophore as shown in figure 3.11(left). And there are power dependence of the electron recombination from TiO_2 to the chromophore C2P2 as shown in figure 3.11 (right).

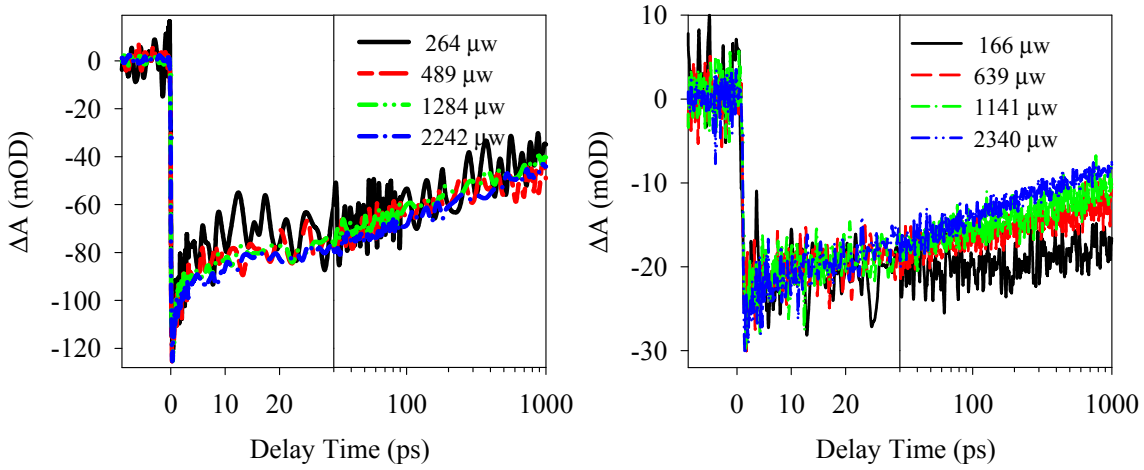

Figure 3.11 The comparison of the C2P2 ground state bleach kinetics of **POM**/C2P2/TiO2 (a) and C2P2/TiO_2 (b) under indicated pump power.

3.3.3 Ions in C2P2 have no effect on the ET from POM to oxidized C2P2

The triad systems with C2P2-2Na^+, C2P2-2Mg^{2+} were measured by the transient

absorption spectroscopy in the visible region. The spectra were almost the same as the system without cations. The kinetics was compared as shown in figure_S8. It indicates that electron transfer rates from the **POM** to C2P2 are independent to the cations in the crowns. Although C2P2 can capture cations and affects the loading of POM onto C2P2, the electron transfer rates from POM to C2P2 were not obviously affected.

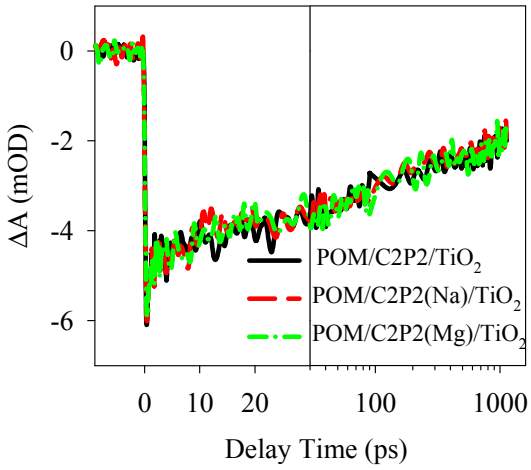

Figure 3.12 The comparison of the C2P2 ground state bleach kinetics of **POM**/C2P2/TiO2 (the black line), **POM**/C2P2-2Na^{+}/TiO2 (the red line) and **POM**/C2P2-2Mg^{2+}/TiO2 (the green line)

3.3.4 Loading Dependence of the Triad

The triad systems with different loading of **POM** show different C2P2 ground state recover rates. As shown in table 3.1, four sets of samples were made with increased **POM** / C2P2 ratio. With higher POM/C2P2 ratio, the ground state recovery rates of C2P2 increased until saturated as shown in figure 3.13. It indicates the electron transfer rates from POM to oxidized C2P2 depend on the POM loading. In addition we have the evidence that there is no ion effect on the electron transfer rate as proved in 3.3.3.

#	Name	Abs (POM)	Abs (C2P2)	Abs (TiO2)	POM/C2P2
S1	**C2P2**	**0.19**	**0.2**	**0.28**	**3.49 : 1**
S2	**C2P2**	**0.32**	**0.17**	**0.3**	**6.91 : 1**
S3	**C2P2(Na)**	**0.54**	**0.19**	**0.31**	**10.4 : 1**
S4	**C2P2(Na)**	**0.76**	**0.17**	**0.31**	**16.4 : 1**

Table 3.1 UV-Vis absorption signal value at 450 nm of samples in loading dependence experiment

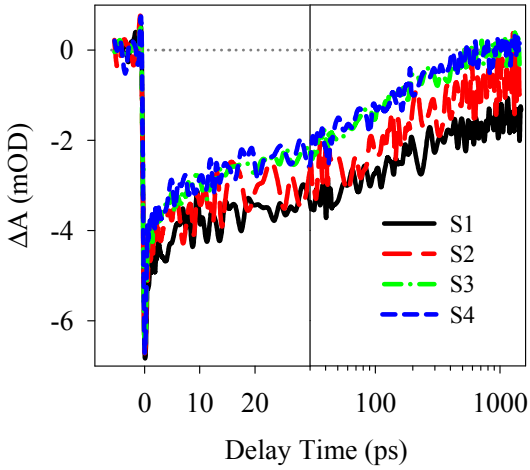

Figure 3.13 The comparison of the C2P2 ground state bleaches on POM/C2P2/TiO_2 films averaging from 470nm to 475 nm with different POM loadings.

3.4 Summary

In this report, we have studied the ultrafast electron transfer dynamics in C2P2 aqueous solution, C2P2/TiO_2, **POM**/C2P2/TiO_2 systems using transient absorption spectroscopy in the visible region and the mid IR region. Our results indicate that the

electron transfer rate from C2P2 to TiO_2 is fast with a weighted lifetime of 95 ps, while the charge recombination rate is relatively slow with a half lifetime of 1.3 us. The transient absorption studies of **POM**/C2P2/TiO_2 show fast ground state recoveries and indicate the electron transferring from the **POM** to the oxidized C2P2. Furthermore, we show that in the presence of **POM** the population of electrons injected into TiO_2 is decreased due to the competitive pathways induced by ligand. In addition, parameters effects of the systems were analyzed, such as pH dependence, power dependence, loading dependence and so on.

References

1 Geletii, Y. V. *et al.* An all-inorganic, stable, and highly active tetraruthenium homogeneous catalyst for water oxidation. *Angew. Chem.-Int. Edit.* **47**, 3896-3899, doi:10.1002/anie.200705652 (2008).

2 Besson, C. *et al.* Cs(9) (gamma-PW(10)O(36))(2)Ru(4)O(5)(OH)(H(2)O)(4) , a new all-inorganic, soluble catalyst for the efficient visible-light-driven oxidation of water. *Chem. Commun.* **46**, 2784-2786, doi:10.1039/b926064a (2010).

3 Huang, Z. Q. *et al.* Efficient Light-Driven Carbon-Free Cobalt-Based Molecular Catalyst for Water Oxidation. *J. Am. Chem. Soc.* **133**, 2068-2071, doi:10.1021/ja109681d (2011).

4 Geletii, Y. V. *et al.* Structural, Physicochemical, and Reactivity Properties of an All-inorganic, Highly Active Tetraruthenium Homogeneous Catalyst for Water Oxidation. *J. Am. Chem. Soc.* **131**, 17360-17370, doi:10.1021/ja907277b (2009).

5 Geletii, Y. V. *et al.* Homogeneous Light-Driven Water Oxidation Catalyzed by a Tetraruthenium Complex with All Inorganic Ligands. *J. Am. Chem. Soc.* **131**, 7522-+, doi:10.1021/ja901373m (2009).

6 Asbury, J. B. *et al.* Femtosecond IR study of excited-state relaxation and electron-injection dynamics of Ru(dcbpy)(2)(NCS)(2) in solution and on nanocrystalline TiO2 and Al2O3 thin films. *J. Phys. Chem. B* **103**, 3110-3119, doi:10.1021/jp983915x (1999).

Chapter 4:

Study the Electron Transfer of Organometallic-Redox Assemblies

4.1 Transient Absorption Spectra and Kinetics[1]

The splitting of H_2O consists of two half reactions: water oxidation and water reduction. Both reactions proceed through multiple proton-coupled electron transfer steps. Since light-induced redox reactions are monoelectronic, an effective water splitting catalyst is necessary to perform as a redox mediator for multielectron transfer[2,3]. Inorganic building blocks, polyoxometalates (POMs) are great candidates as they present various properties such as redox activity,[4,5] photochromism[6]. They have been extensively combined with organic donors and transition metal complexes to form hybrid systems toward multifunctional materials[1].

In this part, the internal electron transfer of the covalent POM–photosensitizer multifunctional molecules (K-Si, K-Sn, D-Si, D-Sn structures see chapter 2.2) which were synthesized by Anna Proust Group[1] were studied and analyzed. Transient absorption apectra of these four molecules in DMF are measured and analyzed. As the control sample, the Ir photosensitizer was measured at the same condition as shown in figure 4.1(left). There are two feature peaks, the peaks at 500nm are assigned to the excited states of Ir while the excited electrons localized on ppy (Ir*); the peaks at 632-642 nm are assigned to the excited states of Ir while the excited electrons localized on the conjugated picolinate moiety (Ir**); the peaks at 700nm are assigned to the reduced POM as shown in figure 4.4 the black lines. By global fitting the kinetics of Ir photosensitizer at 632-642 nm and 700nm as shown in figure 4.1 (right), the internal conversion from Ir* to Ir** was with a weighted lifetime of 4.9ns and the decay of Ir** was with lifetime of 16.8ns as shown in scheme 4.1. The fitting formula is shown below and the derivation of the fit equation is shown in the section4.2.

$$\Delta A = -A \times \left[B \times e^{-\frac{t}{t1}} + (1-B) \times e^{-\frac{t}{t2}} \right] + C \times e^{-\frac{t}{t3}}$$

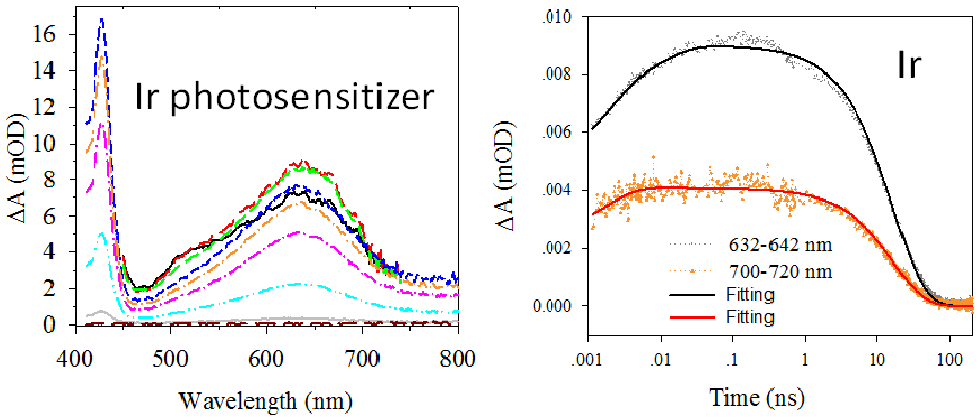

Figure 4.1 (left)the transient absorption spectra of Ir photosensitizer, pumped at 400 nm. (right) the kinetics of the Ir photosensitizer spectra and the fitting line

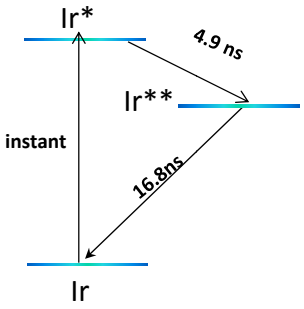

Scheme 4.1 The Schematic electron transfer process of Ir photosensitizer

The transient spectra of the four organometallic-redox assemblies are shown in the figure 4.2. The assignments of the spectra are the same. By global fitting the data as shown in figure 4.3, the electron transfer rate and the process of the four compounds are shown in scheme 4.2. The fitting equation is shown below and the derivation of the equation is shown in the section 4.2

$$\Delta A = -A \times \left[B \times e^{-\frac{t}{t1}} + (1-B) \times e^{-\frac{t}{t2}} \right] + (C-D) \times e^{-\left(\frac{t}{t3}+\frac{t}{t4}\right)} + D \times e^{-\frac{t}{t5}} + E$$

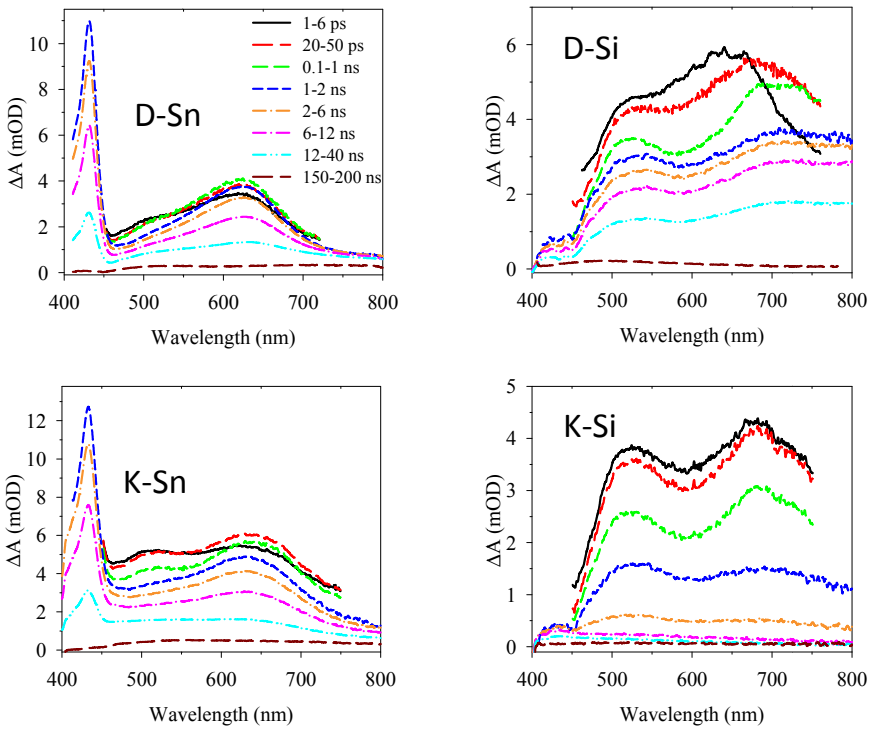

Figure 4.2 (left)the transient absorption spectra of the covalent POM–photosensitizers

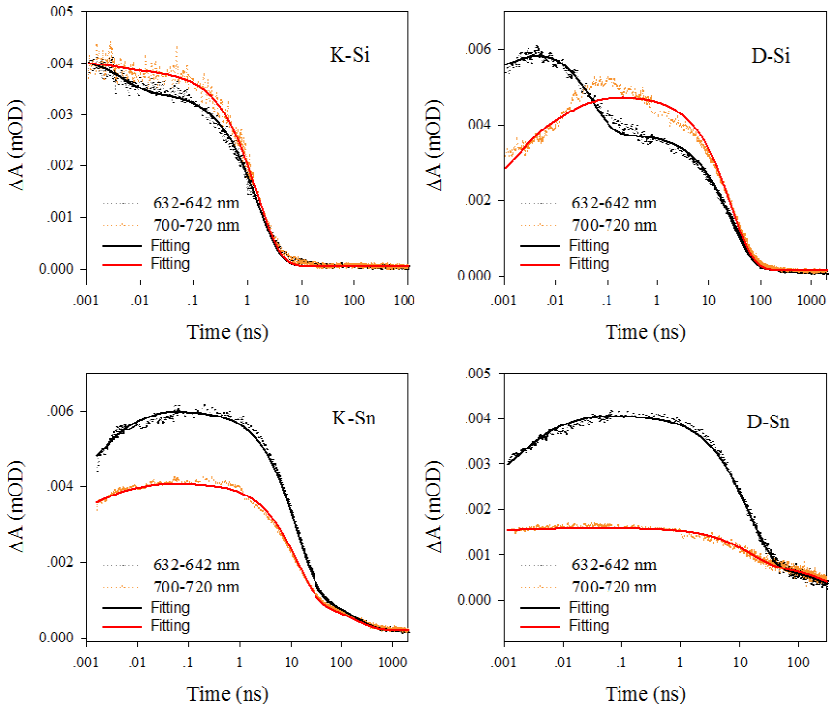

Figure 4.3 (right) the kinetics of the covalent POM–photosensitizers

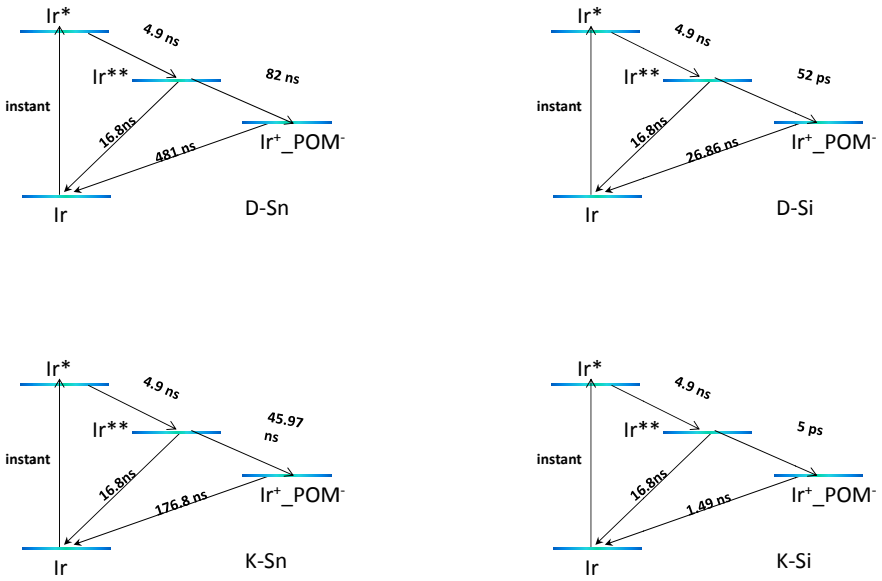

Scheme 4.2 The Schematic electron transfer process of the covalent POM–photosensitizers

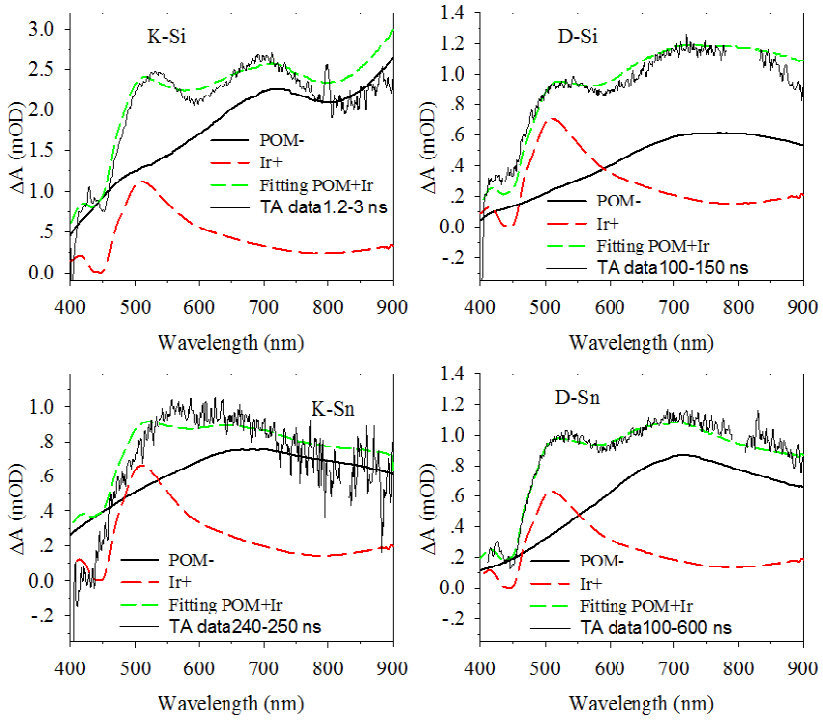

Figure 4.4 Comparison of the transient absorption spectra at indicated delay time and simulated spectra of charge separated states(oxidized iridium and mon-reduced POM).

4.2 Global fitting and explanations[1]

Derivation of the fit equation

The fit equation was derived according to the typical model of electron transfer process.

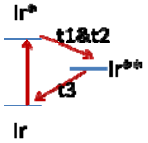

For the Ir photosensitizer

The Population of excited π* [phenylpyridyl (C^N)]: $N^{*}(t)=N_0\left[a_1\times e^{-t/t1}+(1\text{-}a_1)\times e^{-t/t2}\right];$

The Population of excited π* [pyridylcarboxylate (O^N)]:

$N^{**}(t)=N_0\left\{-\left[a_1\times e^{-t/t1}+(1\text{-}a_1)\times e^{-t/t2}\right]+e^{-(t/t3+t/t4)}\right\};$

The absorption signal of 632 nm as an example:

$\Delta A=\epsilon_{632}{}^{*}\times N^{*}(t)+\epsilon_{632}{}^{**}\times N^{**}(t);$

$\Delta A=\epsilon_{632}{}^{*}\times N_0\left[a_1\times e^{-t/t1}+(1\text{-}a_1)\times e^{-t/t2}\right]+\epsilon_{632}{}^{**}\times N_0\left\{-\left[a_1\times e^{-t/t1}+(1\text{-}a_1)\times e^{-t/t2}\right]+e^{-t/t3}\right\};$

$\Delta A=(\epsilon_{632}{}^{*}-\epsilon_{632}{}^{**})\times N_0\left[a_1\times e^{-t/t1}+(1\text{-}a_1)\times e^{-t/t2}\right]+\epsilon_{632}{}^{**}\times N_0 e^{-t/t3};$

We use the fit equation: $\Delta A=-A\times[B\times e^{-\frac{t}{t1}}+(1-B)\times e^{-\frac{t}{t2}}]+C\times e^{-\frac{t}{t3}};$

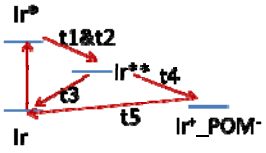

For the hybrids:

The Population of excited π* [(C^N)]: $N^{*}(t)=N_0\left[a_1\times e^{-t/t1}+(1\text{-}a_1)\times e^{-t/t2}\right];$

The Population of excited π* [(O^N)]: $N^{**}(t)=N_0\left\{-\left[a_1\times e^{-t/t1}+(1\text{-}a_1)\times e^{-t/t2}\right]+e^{-(t/t3+t/t4)}\right\};$

The Population of the charge separated Ir^{+}-POM^{-}: $N^{+-}(t)=\frac{1/t3}{1/t3+1/t4}N_0\left[-e^{-(t/t3+t/t4)}+e^{-t/t5}\right];$

The absorption signal of 632 as an example:

$\Delta A=\epsilon_{632}{}^{*}\times N^{*}(t)+\epsilon_{632}{}^{**}\times N^{**}(t)+\epsilon_{632}{}^{+-}\times N^{+-}(t);$

$\Delta A=\epsilon_{632}{}^{*}\times N_0\left[a_1\times e^{-t/t1}+(1\text{-}a_1)\times e^{-t/t2}\right]+\epsilon_{632}{}^{**}\times N_0\left\{-\left[a_1\times e^{-t/t1}+(1\text{-}a_1)\times e^{-t/t2}\right]+e^{-(t/t3+t/t4)}\right\}$

$+\epsilon_{632}{}^{+-}\times\frac{1/t3}{1/t3+1/t4}N_0\left[-e^{-(t/t3+t/t4)}+e^{-t/t5}\right];$

$\Delta A=(\epsilon_{632}{}^{*}-\epsilon_{632}{}^{**})\times N_0\left[a_1\times e^{-t/t1}+(1\text{-}a_1)\times e^{-t/t2}\right]+(\epsilon_{632}{}^{**}\text{-}\epsilon_{632}{}^{+-}\times\frac{1/t3}{1/t3+1/t4})\times N_0 e^{-(t/t3+t/t4)}$

$+\epsilon_{632}{}^{+-}\times\frac{1/t3}{1/t3+1/t4}N_0 e^{-t/t5};$

We use the fit equation: $\Delta A=-A\times[B\times e^{-\frac{t}{t1}}+(1-B)\times e^{-\frac{t}{t2}}]+(C\text{-}D)\times e^{-(\frac{t}{t3}+\frac{t}{t4})}+D\times e^{-\frac{t}{t5}}+E;$ (E for the impurity of the samples)

Reference

1 Matt, B. *et al.* Long lived charge separation in iridium(iii)-photosensitized polyoxometalates: synthesis, photophysical and computational studies of organometallic-redox tunable oxide assemblies. *Chemical Science* **4**, 1737-1745 (2013).

2 Krasna, A. I. Proflavin catalyzed photoproduction of hydrogen from organic compounds. *Photochemistry and Photobiology* **29**, 267-276 (1979).

3 DOUGLAS, J. R. D. P., HARRIMAN, A., PORTER, G. & RICHOUX, M.-C. METAL PHTHALOCYANINES AND PORPHYRINS AS PHOTOSENSITIZERS FOR REDUCTION OF WATER TO HYDRO-GEN. *Coordination Chemistry Reviews* **44**, 83-126 (1982).

4 Harriman, A. *et al.* Intramolecular Electron Transfer Reactions Observed for Dawson-Type Polyoxometalates Covalently Linked to Porphyrin Residues. *The Journal of Physical Chemistry C* **113**, 5834-5842 (2009).

5 Elliott, K. J. *et al.* A porphyrin–polyoxometallate bio-inspired mimic for artificial photosynthesis. *Physical Chemistry Chemical Physics* **11**, 8767-8773 (2009).

6 AlDamen, M. A. *et al.* Mononuclear lanthanide single molecule magnets based on the polyoxometalates [Ln (W5O18) 2] 9− and [Ln (β2-SiW11O39) 2] 13−(LnIII= Tb, Dy, Ho, Er, Tm, and Yb). *Inorganic chemistry* **48**, 3467-3479 (2009).